VOL. 3, NO. 1, JAN.-FEB. 1980 J. GUIDANCE AND CONTROL 11

ARTICLE NO. 78-1311R

Control System Design of the Annular Suspension and Pointing System

David C. Cunningham,* Thomas P. Gismondi,† and George W. Wilson‡
Sperry Flight Systems, Phoenix, Ariz.

This paper presents the control system design for the Annular Suspension and Pointing System intended for use on Shuttle-carried experiment packages in the 1980's. Actuator sizing and configuration of the system are explained, and the control laws developed for linearizing and compensating the magnetic bearings, roll induction motor, and gimbal torquers are given. Decoupling, feedforward, and error compensation for the vernier and gimbal controllers are developed.

Introduction

SOLAR, stellar, and Earth viewing experiments planned for the 1980's require better pointing accuracy and stability than provided by the Space Shuttle attitude control system. Consequently, the need for a multipurpose experiment pointing system was established during NASA planning activities in the early 1970's. The Annular Suspension and Pointing System (ASPS) concept was developed to meet this need. The concept is a derivative of the Annular Momentum Control Device (AMCD), which is described in Ref. 1. A more detailed description of the ASPS and linear analyses are presented in Ref. 2. Although the AMCD and ASPS each utilize the magnetic suspension technique, they are very different in purpose and operation. The ASPS is considered a unique device and has been patented by NASA.[3] A more detailed discussion of the evolution of the ASPS concept that has led to a decision by NASA to build a prototype ASPS for use on the Space Shuttle is presented in Ref 4.

Experiment pointing systems other than ASPS have also been studied to accommodate the wide range of experiment sizes and operational requirements.[5] The ASPS represents a unique approach in that magnetic actuators are used to provide a fully levitated payload mounting base which is isolated from Orbiter disturbances. In addition to the magnetically suspended vernier system, two coarse gimbals, a strapdown attitude determination system, experiment power and signal interfacing electronics, and standard Spacelab interface electronics are included in the ASPS.

Considerable analyses, simulation, and prototype testing have already been performed in support of the system design presented here. In particular, a detailed nonlinear digital simulation of the ASPS dynamics based on the formulation developed in Ref. 4 has been used to verify pointing system performance and actuator sizing. The computational algorithms for the attitude determination system, command processor, and attitude control system have been exercised in another digital simulation, which employs a simplified representation of the ASPS dynamics. System stability margins have been computed using a linearized model of the system, which includes structural flexibility between mast, gimbals, vernier, and the experiment.

Presented as Paper 78-1311 at the AIAA Guidance and Control Conference, Palo Alto, Calif., Aug. 7-9, 1978; submitted Sept. 20, 1978; revision received June 25, 1979.

Index categories: Spacecraft Systems; Sensor Systems.

*Lead Engineer, Satellite Systems Development Dept. Member AIAA.

†Principal Engineer, Satellite Systems Development Dept.

‡Staff Engineer, Satellite Systems Development Dept. Member AIAA.

Control Requirements

Major control system requirements of the ASPS are listed in Table 1.

The pointing accuracy and stability requirements apply during inertial pointing and assume ideal payload attitude and rate sensing. The payload mass and inertia values listed are those which apply to the acceleration and bandwidth requirements. Large payloads (up to 800-kg mass, 1000 kg-m^2 inertia normal to LOS and 250 kg-m^2 inertia along LOS) must also be accommodated, but at reduced acceleration during slewing maneuvers.

The driving requirements affecting ASPS system design have been the vernier pointing stability (which necessitates high linearity and close calibration of the magnetic actuators) and the roll rate stability (which demands extremely low anomaly torques in the roll actuator system).

In addition to the performance requirements given, several configuration-related requirements have been imposed. The vernier control system must provide noncontacting suspension of the payload using magnetic actuators without permanent magnets. (The restriction against permanent magnets avoids the need for high-bandwidth servos to stabilize the static instabilities inherent with permanent magnet actuators.) The ASPS must provide power and data support to the payload and be compatible with the Orbiter environmental, operational, and safety requirements. Electrical power and data interfaces must be compatible with the Spacelab. A payload mounting plate should be provided for convenient payload integration, and its diameter should not exceed 1 m. A NASA standard digital computer (the NSSC-II) and inertial reference unit (the DRIRU-II) will provide a strapdown attitude reference for the payload. The system segmentation should take advantage of the computer to perform all of the mission-dependent control law computations.

Hardware Description

The ASPS consists of a vernier pointing assembly, lateral and elevation gimbal assemblies, a mounting and jettison assembly, several control electronics assemblies, the NSSC-II digital computer, and the DRIRU-II inertial reference unit (IRU). Figure 1 shows the ASPS mechanical layout. Two identical coarse gimbal assemblies are stacked to form an elevation and a lateral gimbal pair. The gimbal mounting structure design provides a mechanically limited travel of ±100 deg (from vertical) about the lower elevation gimbal

Table 1 ASPS control requirements

Requirement	Value	Units
Vernier pointing/isolation system		
Angular range	±0.75	deg
Pointing accuracy	±0.1	arc-sec
Pointing stability	±0.01	arc-sec
Bandwidth	1.0	Hz
Payload mass (max.)	600	kg
Payload inertia (perpendicular to LOS)	50 to 500	kg-m^2
Payload c.m. offset (along LOS)	0 to 1.5	m
Roll pointing system		
Angular range	unlimited	...
Acceleration (max.)	±0.06	deg/s^2
Rate (max.)	±1.5	deg/s
Pointing accuracy	±1.0	arc-sec
Rate stability	±1.0	arc-sec/s
Bandwidth	1.0	Hz
Payload inertia (about LOS)	10 to 100	kg-m^2
Elevation and lateral coarse gimbals		
Elevation range	±100	deg
Lateral range	±60	deg
Maximum rate	±3	deg/s
Maximum acceleration	±2000	arc-sec/s^2
Position accuracy	±6	arc-min
Rate accuracy	±0.03	deg/s

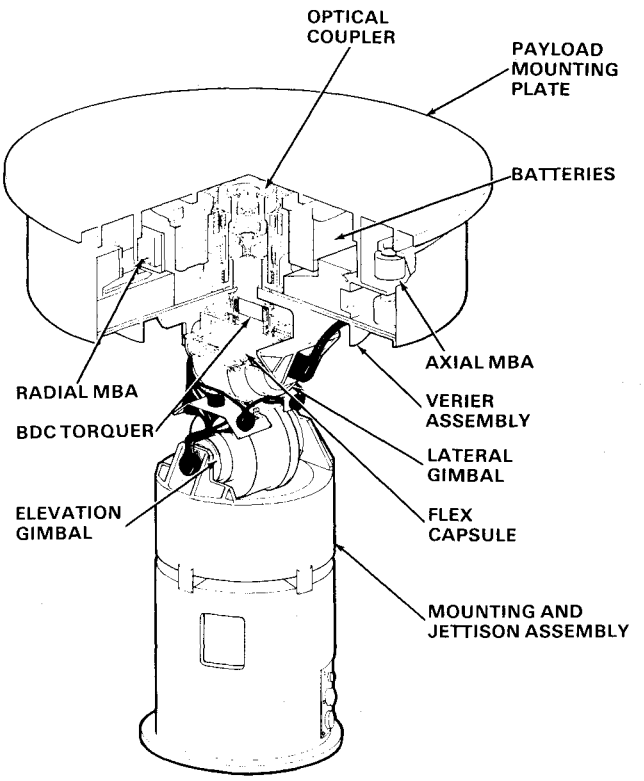

Fig. 1 ASPS layout.

axis, and ±60 deg about the upper gimbal axis. Soft stops can be adjusted during mission integration to further limit the gimbal travel. The vernier pointing assembly contains the roll axis drive, which provides unlimited rotation about the payload longitudinal axis and magnetic actuators for vernier rotation up to ±0.75 deg about any axis in the plane normal to the payload roll axis. The payload mounting plate can be removed for mounting and aligning experiments prior to installation on the ASPS.

Magnetic suspension provides noncontacting isolation and vernier positioning of the payload in the vernier assembly. Three axial magnetic bearing assemblies (MBA's) provide axial translation and vernier pointing about the transverse axes. Proximeters associated with each MBA linearize the force/displacement characteristic to compute the axial displacement and the tilt of the payload about the transverse axes.

The axial MBA's react against the horizontal surface of an L-shaped soft iron rotor which runs circumferentially under the payload plate mounting surface at a mean radius of 0.362 m. The vertical surface of this rotor is utilized by the two radial MBA's and the single roll motor. The radial MBA's are spaced 90-deg apart and provide radial centering of the payload mounting plate. Each radial MBA contains proximeters for magnetic gap compensation and for centering.

A segmented, two-phase, solid-iron rotor, ac induction motor controls the roll rotational servo. This motor also contains proximeters to compensate the radial attractive force associated with the two motor segments. Roll angular position is sensed by a single-speed wound rotor resolver located near the center. Resolver rotor signals are ac coupled to the stationary side of the assembly through a rotary transformer.

In addition to the six-degree-of-freedom positioning and readout provided by the vernier assembly, power, control, and data transfer to the payload experiment are also supplied. Twenty-three nickel-cadmium cells, mounted below the rotating top plate, supply 300 W-h of energy to the experiment. To recharge the batteries, the vernier is caged by energizing five solenoid actuated latches. A solenoid-operated brush block assembly is then engaged with the vernier slip rings to connect power and battery charge signals directly to the payload plate. The vernier latch mechanisms permit the use of the ASPS in a coarse pointing mode for comparison with the vernier system or as a backup. Additionally, the latches are designed so that a failure within the magnetic suspension causes the suspended assembly to touch down on the latches, thereby protecting the MBA's, proximeters, etc.

An optical coupling technique transfers experiment control and data signals across the vernier gap. Three serial data channels are provided, with one uplink and one downlink channel used to extend the Spacelab experiment data bus to a standard remote acquisition unit (RAU) located on the payload mounting plate. The second downlink transfers IRU data to the ASPS control electronics and supports wideband experiment data transfer to the Spacelab high-rate multiplexer.

Each of the coarse gimbal assemblies contain a permanent magnet, brushless two-phase dc torquer, a multispeed wound rotor resolver for commutation of the torquer drive signal and a single-speed wound rotor resolver for position readout and control of the gimbal angle. Since both elevation and lateral gimbals have a limited rotational freedom, electrical connections are carried across the rotating gimbals through flex capsules. The flex capsules contain flat flex tapes which are looped between concentric cylinders in the center of each gimbal. Cabling is sized to support all of the coarse and vernier signal and power requirements as well as high-speed payload data and battery recharge power. Duplex gimbal bearing pairs are used in each gimbal assembly in a fixed/floating cartridge arrangement. The cartridges permit the bearing preload to be set by tolerances within the cartridge itself; dimensional changes which result from temperature variations cause the sliding cartridge to move axially without inducing mechanical stresses or upsetting the bearing preloads.

The mounting and jettison assembly supports the coarse gimbals and also contains pyrotechnics to jettison the ASPS (and payload) in the event of a multiple failure which prevents stowage in orbit. A motor-driven separation device mounted

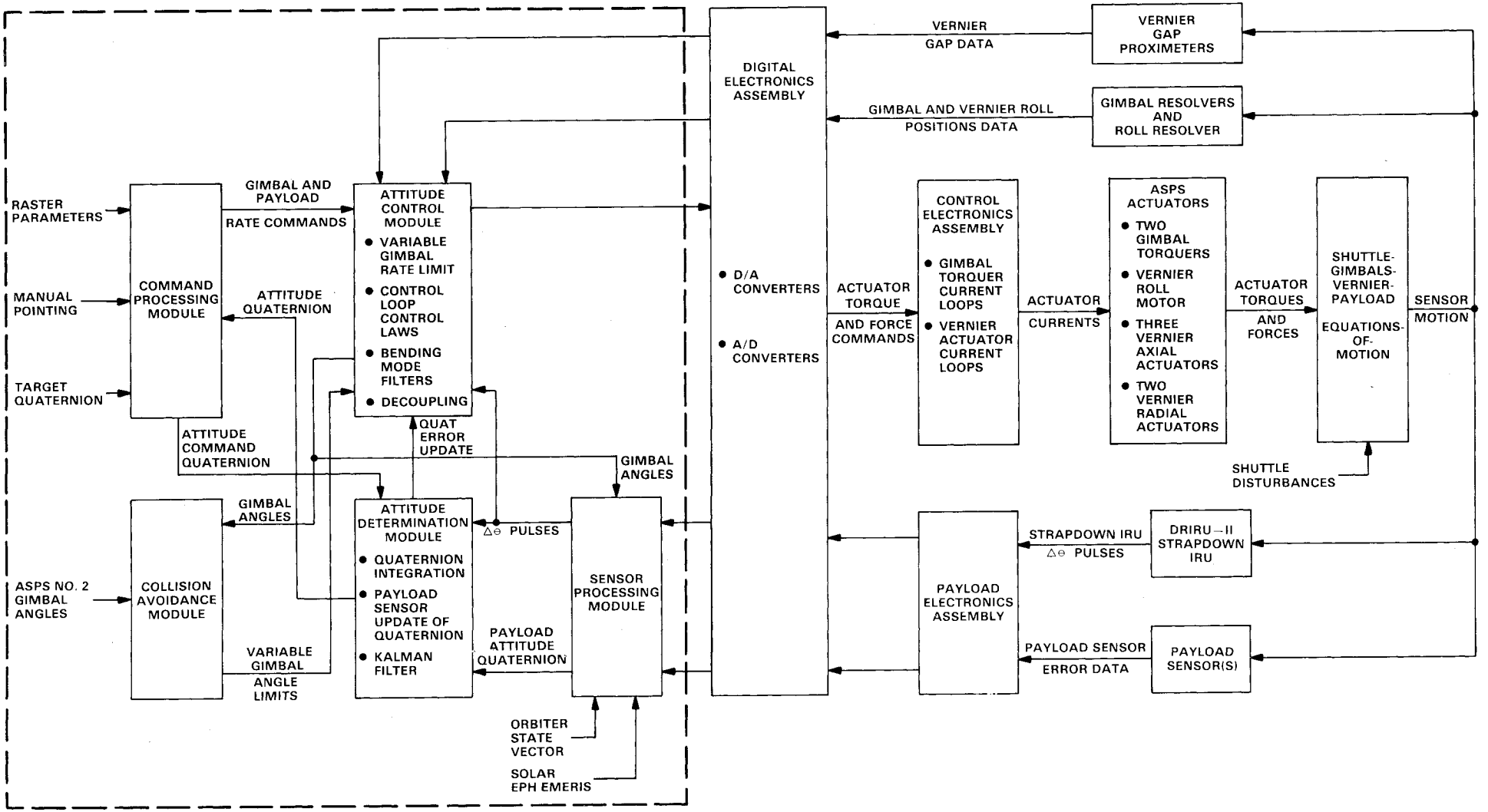

Fig. 2 Control system block diagram.

Table 2 ASPS characteristics

Power	
Standby	77 W
Average	89 W
Peak (worst case)	1100 W
Weight	
Mechanical	240 kg (530 lb)
Control electronics	40.8 kg (90 lb)
Digital computer and IRU	30.8 kg (68 lb)
Size	
Vernier system height	0.241 m (9.5 in.)
Overall height	1.174 m (46.3 in.)
Payload plate diameter	0.965 m (38 in.)

inside the mounting and jettison assembly disconnects the gimbal mechanical structure from the mast during launch and landing phases. This prevents indeterminant loading across the gimbals when the payload is restrained by its launch locks.

Table 2 lists the overall characteristics of the ASPS. The peak power of 1100 W is a worst-case combination of maximum force and torque by all actuators simultaneously.

Control System Configuration

The ASPS control system configuration block diagram is presented in Fig. 2. The left side of the block diagram shows the five NSSC-II software modules, which are directly related to the ASPS attitude control system (ACS). The right side of the block diagram shows the hardware elements of the ACS. The major functions of some of the blocks are listed within the blocks.

The three electronic assembly boxes are the digital electronics assembly (DEA), the payload electronics assembly (PEA), and the control electronics assembly (CEA). The major function of the DEA is to interface the NSSC-II computer with the PEA, CEA, and ASPS coarse gimbal and vernier sensors. All interface is accomplished through I/O modules which provide signal conditioning, formatting, and encoding required to render external signals compatible with the DEA internal bus and the 12-bit D/A and A/D converters.

The primary function of the PEA is to interface the ASPS inertial sensors such as the DRIRU-II, fine sun sensor, STELLAR star tracker, and other experiment-provided sensors. Data from the sensors is encoded by the PEA and transmitted to the DEA, which is remotely located from the ASPS payload plate. The sequence of the data is determined by a microprocessor in the PEA.

The major function of the CEA is to provide the analog circuits required for the ASPS control loops. This includes excitation of the brushless dc gimbal torquer commutation resolvers, gimbal torquer current loops, and gimbal position sensor resolver excitation and output demodulation.

The gimbal resolvers are the sensors for the coarse gimbal control loops. The vernier roll resolver and gap proximeters are the sensors used to control the payload plate roll angle and keep the payload plate centered in the gap. The DRIRU-II strapdown IRU is the short-term inertial reference; the payload sensor(s) provides the long-term inertial reference.

The $\Delta\theta$ pulse outputs from the DRIRU-II go directly to the NSSC-II attitude control module software where they serve as the attitude error signal in the software fast loop which has a 0.020-s frame time. The $\Delta\theta$ pulse outputs also go to the software attitude determination module where they are the inputs to a quaternion integration algorithm which gives the ASPS payload attitude in a unit quaternion format. The quaternion integration is performed at a slow loop frame time of 1 s. The attitude error obtained from the attitude determination module is used to correct the attitude control module attitude error obtained directly from the IRU $\Delta\theta$ pulses. A Kalman filter in the attitude determination module provides an optimal estimate of the three-body axis attitude errors and the three-body axis drift rates. It provides for payload sensor updates of the quaternion obtained by integration of the IRU $\Delta\theta$ pulses and accounts for the sensor noise.

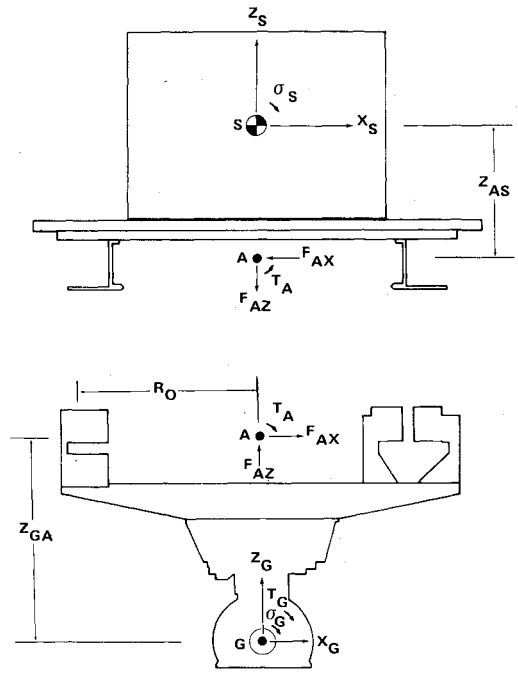

Fig. 3 Simplified ASPS planar model geometry.

A complete description of all of the portions of the ASPS control system shown in Fig. 2 is not within the scope of this paper. This paper emphasizes the ASPS hardware, magnetic actuator linearization, and the software attitude control module functions. The reader is referred to Ref. 6 for the discussions of the basic attitude determination system, the command processing, and items related to the digital implementation of the attitude control system.

Actuator Sizing

Sizing of the coarse gimbal torquers as well as the vernier assembly magnetic actuators is based on the slew acceleration requirement of 2000 arc-sec/s^2. Figure 3 shows a simple planar representation of a rigid ASPS/payload combination.

The free-body dynamics are simply

$$M_S\ddot{X}_S = -F_{AX} \tag{1a}$$

$$M_S\ddot{Z}_S = -F_{AZ} \tag{1b}$$

$$I_S\ddot{\sigma}_S = -T_A + Z_{AS}F_{AX} \tag{1c}$$

$$I_G\ddot{\sigma}_G = -T_G + T_A + Z_{GA}F_{AX} \tag{1d}$$

For an aligned slew consisting of an angular gimbal acceleration, $\ddot{\sigma}_G$,

$$\ddot{X}_S = (Z_{GA} + Z_{AS})\ddot{\sigma}_G \tag{2a}$$

$$\ddot{Z}_S = 0 \tag{2b}$$

$$\ddot{\sigma}_S = \ddot{\sigma}_G = 2000 \text{ arc-sec/s}^2 \tag{2c}$$

Since the slew can occur about any axis in the plane normal to the payload line of sight, the peak force required of the radial and axial actuators is

$$F_{\text{radial}} = |F_{AX}| \tag{3a}$$

$$F_{\text{axial}} = |F_{AZ}|/3 + |T_A|/2R_0 \tag{3b}$$

Table 3 Actuator size requirements

Actuator	Min. rqt.	Actual	Units
Radial MBA	11.5	14.2	N
Axial MBA	30.2	34.3	N
Lateral torquer	22.5	33.9	N-m
Elevation torquer	27.2	33.9	N-m
Roll motor	0.574	0.678	N-m

Combining Eqs. (1-3) and substituting nominal values for M_S (645 kg), I_S (597 kg-m^2), I_G (20.7-kg-m^2 elevation, 7.3-kg-m^2 lateral), Z_{AS} (1.395 m), R_0 (0.362-m), and Z_{GA} (0.445-m elevation, 0.235-m lateral), the minimum actuator sizes listed in Table 3 are easily obtained. The actual capabilities are somewhat larger. It is also apparent that actuator force and torque requirements are minimized by maximizing the radial distance R_0 and minimizing the gimbal offset Z_{GA}. The selected dimensions fulfill this optimization within the constraints of a 1-m vernier diameter, realistic torque motor aspect ratio, and practical mechanical structure.

Roll motor sizing is determined simply by the acceleration required to provide the 1-Hz bandwidth at an amplitude of ± 30 arc-sec:

$$T_{\text{roll}} = \psi_{\max}\omega^2 I_{\text{roll}} \tag{4}$$

The selection of three axial actuators, two radial actuators, and a single roll motor segment was made over other arrangments (four axial MBA's, for example) because it minimizes the hardware complexity, the additional control law transformations are easily implemented, and the actuators can be placed in a reasonably balanced arrangement around the vernier. Operational gaps of all of the axial MBA's must be greater than ± 4.74 mm to accommodate the ± 0.75-deg vernier angular range at the rotor radius. A larger gap requires an increase in the MBA cross-sectional area, thereby increasing size and weight. On the other hand, a larger gap permits lower bandwidth operation of the isolation servos which improves pointing stability. An operating gap range of ± 5.08 mm was selected for all of the vernier actuators which permits a low-frequency isolation bandwidth of 0.1 Hz.

Magnetic Bearing Assembly Linearization and Control

The magnetic actuators used for radial and axial suspension are inherently nonlinear devices which require a unique compensation in this application. Figure 4 shows the geometry associated with each electromagnet. The soft iron rim is attracted to coils 1 and 2 by forces F_1 and F_2, respectively. Each coil is characterized by the equivalent circuit indicated on the figure. The net force can be found from the coenergy associated with the flux linkage between stator and rotor.

$$F = \frac{1}{2}\frac{d}{dg}\left[\frac{L_G I_1^2}{(1-\Delta g/g_0)} + \frac{L_G I_2^2}{(1+\Delta g/g_0)}\right]$$

$$= \frac{K}{g_0^2}\left[\frac{I_1^2}{(1-\Delta g/g_0)^2} - \frac{I_2^2}{(1+\Delta g/g_0)^2}\right] \tag{5}$$

where the actuator constant is $K = (L_G g_0/2)$.

Note that the force is proportional to the square of the coil currents and is inversely proportional to the square of the distance to each coil. To remove the current-squared nonlinearity, a bias current technique is used. This consists of adding a bias current to one coil and subtracting the same bias current from the opposite coil.

To compensate for the inverse-gap-squared relationship, the total (bias and command) currents to each coil are

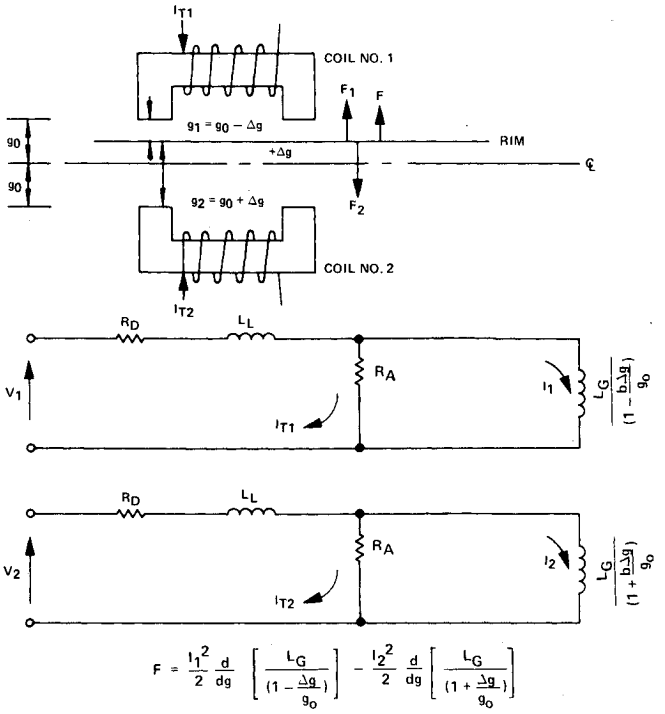

Fig. 4 Magnetic bearing assembly equivalent circuit.

multiplied by signals proportional to the measured gap of that coil:

$$I_{1C} = \left(1-\frac{\Delta g}{g_0}\right)\left[I_0 + \left(\frac{g_0^2}{4KI_0}\right)F_c\right] \tag{6}$$

$$I_{2C} = \left(1+\frac{\Delta g}{g_0}\right)\left[I_0 - \left(\frac{g_0^2}{4KI_0}\right)F_c\right] \tag{7}$$

The magnitude of the bias current determines the scale factor between the current and force; it also affects the power dissipated in the actuator. On ASPS, the bias current was selected to minimize the peak power:

$$I_0 = (g_0/2)\sqrt{F_{\max}/K} \tag{8}$$

This choice has the property that the net current through one coil doubles as the force command increases from zero to maximum, while the current through the opposite coil drops to zero under the same condition. This permits the MBA's to be driven from power amplifiers which do not have to provide bidirectional current outputs. Figure 5 is a block diagam showing the linearization and gap compensation technique.

The preceding discussion applies only to the static force-current-gap characteristics of a magnetic actuator. The dynamic behavior of the bearing must also be compensated by the current loops driving the individual coils. Applying Kirchoff's loop equations to the equivalent circuit of Fig. 4 and differentiating the flux linkage associated with the gap-dependent inductance by parts results in

$$V_1 = R_D I_{T1} + L_L \dot{I}_{T1} + R_A (I_{T1} - I_1) \tag{9}$$

$$O = R_A (I_{T1} - I_1) + \frac{L_G}{(1-\Delta g/g_0)}\dot{I}_1$$

$$+ \frac{I_1 L_G}{(1-\Delta g/g_0)^2}\left(\frac{\Delta \dot{g}}{g_0}\right) \tag{10}$$

$$V_2 = R_D I_{T2} + L_L \dot{I}_{T2} + R_A (I_{T2} - I_2) \tag{11}$$

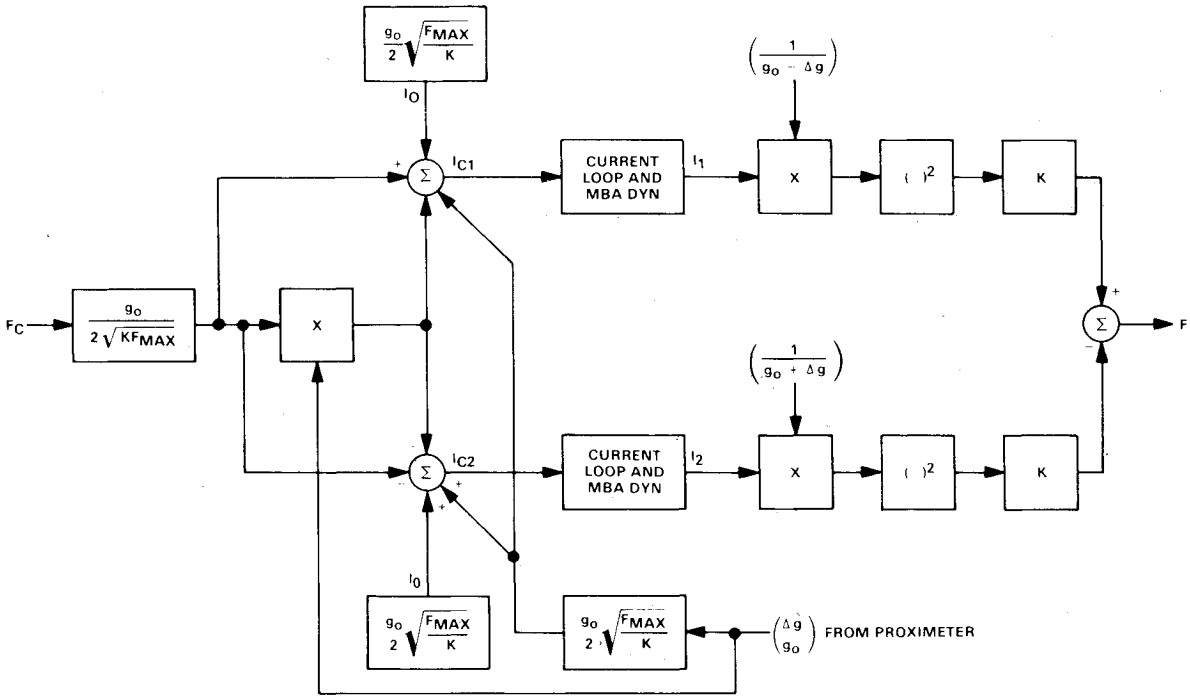

Fig. 5 Block diagram of MBA linearization and gap compensation.

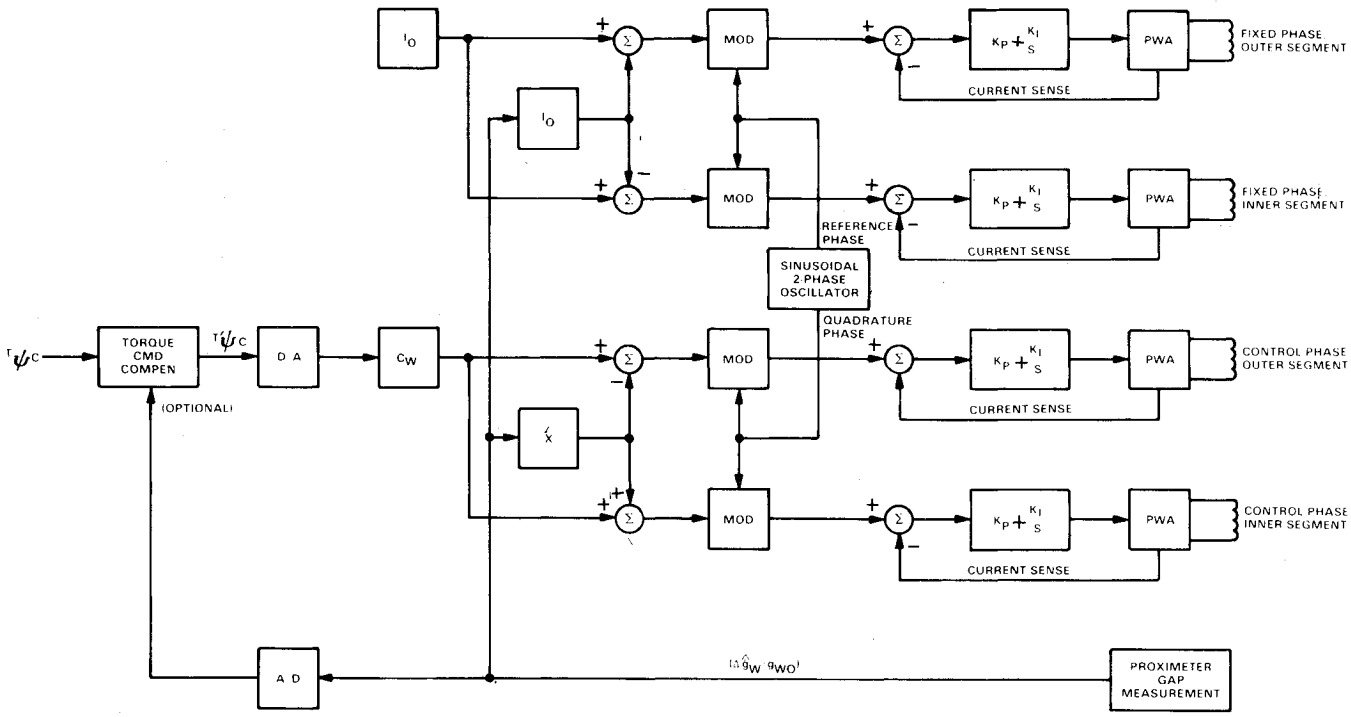

Fig. 6 Roll motor control system.

$$O=R_A(I_{T2}-I_2)+\frac{L_G}{(1+\Delta g/g_0)}\dot{I}_2 - \frac{I_2 L_G}{(1+\Delta g/g_0)^2}\left(\frac{\Delta \dot{g}}{g_0}\right) \tag{12}$$

Examination of these equations reveals the presence of two effects which tend to prevent the currents which create the MBA force (I_1 and I_2) from equalling the controlled (terminal) currents, I_{T1} and I_{T2}. Gap rate causes a speed voltage, while the presence of leakage inductance (L_L) and ac losses (R_A) result in a high-frequency first-order lag between the total current and the magnetizing current. This lag is typically well above the control frequencies of interest on ASPS, and therefore is not compensated.

Considering the gap speed voltage to be a disturbance input, its effect is to create an error in the output force of the actuator. This error is reduced, according to conventional servo theory, by increasing the loop gain ahead of the disturbance input. Two forms of current loop compensator that achieve excellent results are

$$G(s)=K_I[(K_P/K_I)s+1]s^{-1} \tag{13}$$

or

$$G(s)=K_I K_2[(K_I/K_2)s+1][(K_P/K_I)s+1]s^{-2} \tag{14}$$

A typical design procedure, for either compensator, is to select K_P/K_I equal to the coil $(L_L+L_G)/R_D$ time constant, and then select the other parameters for stable operation at the desired bandwidth.

Simulation studies have shown that the gap rate error is reduced below the point where significant pointing error occurs if the bandwidth of the current loop is greater than 800 Hz with a single integrator compensator or 100 Hz with the double integrator compensator. The ASPS design utilizes 500-Hz double integrator current loops.

Roll Motor Linearization and Control

The most severe roll requirement listed in Table 1 is the pointing stability of 1 arc-sec/s which applies to rates up to the maximum of 1.5 deg/s. This corresponds to a rate ripple of 0.0185% and applies to the roll control system when commanded by an ideal roll error sensor. Allowable cogging and torque ripple anomalies in the roll motor can be related to the rate ripple once the servo compensation is determined. For a 1-Hz roll control bandwidth, the maximum motor cogging and ripple are 1.36×10^{-4} N-m (10^{-4} ft-lb) and 0.02%, respectively. The selected roll motor is a two-phase, segmented, solid-iron rotor, ac induction motor, which can provide peak torques of ±0.678 N-m (±0.5 ft-lb). This motor was selected specifically to meet these low-anomaly torque requirements.

The roll motor contains two curved stator segments, which are nominally equidistant from the solid-iron rim. One of these segments is inside the rim and the other is outside the rim and in the same radial direction as the inside segment. Each segment contains a fixed and a control field winding. Both fixed and variable field excitations are controlled using active current control loops. The use of current rather than voltage control is required to effect minimum radial unbalance force from the roll actuators over the full range of radial gap. Since the roll motor segments act like magnetic actuators in the radial direction, it is necessary to modulate both the fixed and variable field currents proportional to the distance between the rotor and each stator segment. This distance is computed from the sensed gap measured by proximeters which are integrally mounted in the motor segments. Since the radial attractive force is proportional to current squared, a force balance can be achieved by causing each stator winding current to vary linearly with its respective gap. This is identical to the MBA gap compensation technique. However, the gap compensated winding commands are ac modulated before they are amplified and applied to the motor windings. The carrier frequency selected for the motor involves a tradeoff between higher power efficiency at lower frequencies and lower residual forces at higher frequencies. A nominal value of 200 Hz has been selected. The current loop design uses straightforward proportional plus integral compensation and has a closed-loop bandwidth of 700 Hz. This bandwidth is well below the pulsewidth-modulation frequency of 10 kHz used in the power stages of the roll drive electronics.

If the radial gap is held fixed, the roll motor operates like a servo induction motor with constant fixed field excitation and a control field excitation which is proportional to the roll torque command $T_{\psi C}$. The developed torque from each segment is proportional to the product of fixed and control field currents in that segment. Phasing is such that the torques from inner and outer segments will add. As the radial gap varies, both fixed and control field currents in inner and outer segments will vary to maintain zero net radial force. Some variation will also occur in the developed torque since the effective motor scale factor is related by the ratio of induced rotor currents to stator winding currents. This ratio will vary with gap to some extent. Tests are currently underway to evaluate this factor. If necessary, the roll motor torque command can be compensated by the radial gap within the software. Figure 6 is a block diagram of the roll motor compensation and drive system including the optional torque command compensation.

Gimbal Torquer Control

Each coarse gimbal contains a permanent magnet brushless dc torque motor capable of producing 33.9 N-m (25 ft-lb) of output torque. The torquers use continuous two-phase winding commutation with sine and cosine phase excitations obtained by passing the torque command through a multispeed resolver mechanically slaved to the torquer. Since the torquer contains 24 poles, a 12-speed resolver is used.

Current loops used in each of the motor phases provide low offsets, good linearity, high bandwidth, and insensitivity to line voltage variations. Since gimbal rates are very low in this application, back emf effects are negligible, and the current loop design can be based on a simple reactance model for the windings. A closed-loop bandwidth of 500 Hz is easily obtained with simple proportional plus integral compensation on the current error signal.

Fine-Pointing Control System

In the fine-pointing mode of operation, the payload is stabilized with respect to an inertially fixed or slowly moving target. The magnetic actuators within the vernier assembly provide the control torques needed to point the experiment; they also provide active low-frequency isolation of translational and rotational forces and moments which result from Orbiter disturbances. These disturbances include the Orbiter vernier reaction control system (VRCS) jet firings and man-motion disturbances. Since the vernier pointing system actuators have an operational range of only ±5 mm, the allowable rotation of the payload about its center of mass or the translation of the Orbiter would be very limited if total inertial stabilization of the payload were achieved. The proximeters located within the vernier assembly are processed to provide a centering function to avoid this limitation.

To explain the control technique used, the simple planar model used to size the actuators may be used (Fig. 3). The dynamics of this system are listed in Eq. (1), and the following control laws may be considered for the four degrees of freedom listed:

$$T_A = -G_A(\sigma_{CMD}-\sigma_S) \tag{15a}$$

$$T_G = G_G(\sigma_S-\sigma_G) \tag{15b}$$

$$F_{AX} = G_{AX}(X_S - Z_{AS}\sigma_S - Z_{GA}\sigma_G) \tag{15c}$$

$$F_{AZ} = G_{AZ}(Z_S) \tag{15d}$$

The payload rotation σ_S is measured using inertial sensors on the payload plate (such as the DRIRU-II) and the remaining terms are measured using the vernier proximeters [$(\sigma_S-\sigma_G)$ = tilt between vernier and gimbal, $(X_S - Z_{AS}\sigma_S - Z_{GA}\sigma_G)$ = radial gap, and Z_S = axial gap]. If these control equations are substituted into Eq. (1), the following system results:

$$I_S s^2\sigma_S = G_A(\sigma_{CMD}-\sigma_S) + Z_{AS}G_{AX}(X_S - Z_{AS}\sigma_S - Z_{GA}\sigma_G) \tag{16a}$$

$$I_G s^2\sigma_G = G_G(\sigma_S-\sigma_G) - G_A(\sigma_{CMD}-\sigma_S) + Z_{GA}G_{AX}(X_S - Z_{AS}\sigma_S - Z_{GA}\sigma_G) \tag{16b}$$

$$M_S s^2 X_S = -G_{AX}(X_S - Z_{AS}\sigma_S - Z_{GA}\sigma_G) \tag{16c}$$

$$M_S s^2 Z_S = -G_{AZ}Z_S \tag{16d}$$

This system is highly coupled due to the offsets between the point of application of the radial centering forces and the

Table 4 Fine-pointing mode control law parameters

Control loop	Bandwidth, Hz	Control law	K_p	K_I	K_R	τ_1	τ_2
Vernier pointing	1	Eq. (18a)	$64I_S$	1	$16I_S$	...	...
Gimbal followup	10	Eq. (18b)	$1024I_G$	16	...	0.0625	0.001
Vernier radial and axial	0.1	Eqs. (18c) and (18d)	$0.1225M_S$	0.175	...	5.972	0.3572

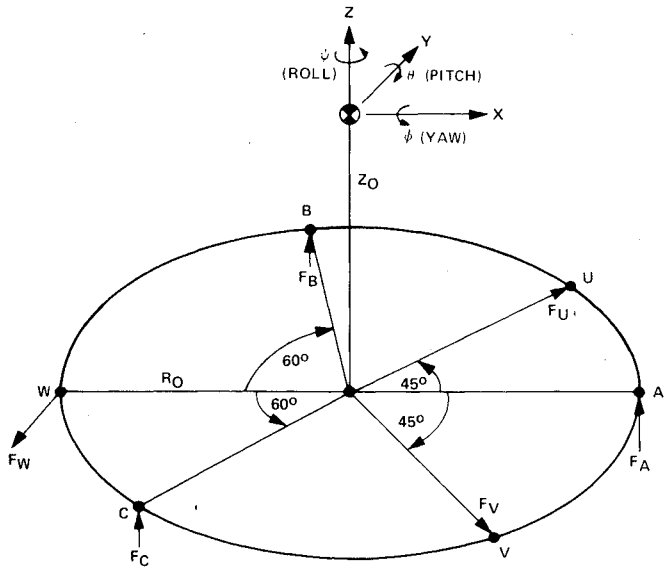

Fig. 7 Vernier actuator and proximeter nomenclature.

rotational centers of the payload and gimbal. Also, the gimbal controller must carry the reaction torques of the vernier actuators. Separation of the control bandwidths of the pointing, centering, and gimbal servo effectively decouples these dynamics at low frequency. However, a transient pointing error will result with this approach, since a finite error must be sensed before the pointing servo can apply a corrective torque. A better approach makes use of the known (or estimated) geometry and the fact that the applied forces and torques are generated electronically and therefore are available for use as decoupling terms in the other control loops. For example, a fully decoupled control policy is

$$T_A = -G_A(\sigma_{CMD} - \sigma_S) + \hat{Z}_{AS}\hat{F}_{AX} \tag{17a}$$

$$T_G = G_G(\sigma_S - \sigma_G) - \hat{T}_A - \hat{Z}_{GA}\hat{F}_{AX} \tag{17b}$$

$$F_{AX} = G_{AX}(X_S - Z_{AS}\sigma_S - Z_{GA}\sigma_G) \tag{17c}$$

$$F_{AZ} = G_{AZ}(Z_S) \tag{17d}$$

The decoupling torques occur in both vernier and gimbal pointing axes. However, only the c.m. offset decoupling in the vernier control is used in ASPS because the gimbal frictional torques will mask the small decoupling torques and because pointing stability of the gimbal coordinate is not important in the fine- (vernier) pointing mode.

Selection of the control law form for G_A, G_G, G_{AX}, and G_{AZ} is based on the type of data sensed (position, rate, or both). Minimum centering bandwidth is determined by the peak centering errors during Shuttle disturbances, and the maximum pointing bandwidth is limited to avoid excitation of the payload structural modes. Control law gain determination is mission dependent in that payload mass, inertia, c.m. offset (actual and estimated), and flexibility characteristics are involved as well as the location of the ASPS within the payload bay and expected disturbances during fine pointing.

Representative designs have been worked out for a number of payloads using a linear system analysis program and a detailed simulation of the ASPS, payload and Orbiter. Typical control laws for the fine-pointing mode are

$$T_A = -K_{PA}[(K_{IA}/S) + 1](\sigma_{CMD} - \sigma_S) + K_{RA}S\sigma_S + \hat{Z}_{AS}\hat{F}_{AX} \tag{18a}$$

$$T_G = K_{PG}\left(\frac{K_{IG}}{S} + 1\right)\left(\frac{\tau_{1G}S + 1}{\tau_{2G}S + 1}\right)(\sigma_S - \sigma_G) \tag{18b}$$

$$F_{AX} = K_{PAX}\left(\frac{K_{IAX}}{s} + 1\right)\left(\frac{\tau_{1AX}S + 1}{\tau_{2AX}S + 1}\right) \times (X_S - Z_{AS}\sigma_S - Z_{GA}\sigma_G) \tag{18c}$$

$$F_{AZ} = K_{PAZ}\left(\frac{K_{IAZ}}{s} + 1\right)\left(\frac{\tau_{1AZ}S + 1}{\tau_{2AZ}S + 1}\right)(Z_S) \tag{18d}$$

The control law gains and time constants for the fine pointing mode are shown in Table 4.

The fine-pointing control developed for the simple planar model may be extended to the actual ASPS. Layout and nomenclature of the proximeters and actuators within the vernier assembly are shown in Fig. 7. The three axial actuators are designated *A, B,* and *C* and are spaced at radius R_0, 120-deg apart. The radial actuators are *U* and *V* and are located ±45 deg from the *A* actuator. Roll torque is produced by a force at point *W*, which is diametrically opposite *A*. The payload c.m. is located at distance Z_0 directly above the center of the vernier actuator plane, and forms the origin of the payload fixed coordinate system, *X, Y, Z*.

The six forces and torques acting on the payload can be expressed in terms of the six actuator forces as indicated on the block diagram of Fig. 8. The inverse relationship which is required for force distribution in the control laws is also shown. The torque coupling resulting from the payload c.m. offset is indicated on the block diagram by the summing functions on the right side. The matrix products shown represent the geometrical layout of the actuators in the plane of the payload rim and are not related to the end mount c.m. offset. Crossfeeding electrical signals proportional to the commanded actuator forces in the control circuitry on the left-hand side of the diagram accomplishes decoupling.

Under the assumption of ideal decoupling, all of Fig. 8 can be condensed to the blocks shown as "decoupled vernier forces" on Fig. 9. This figure also shows the control loops used to provide translational isolation and vernier pointing. Matrix products are indicated in Fig. 9 to obtain the translational gap motions at each actuator which are sensed by the proximeters. The terms ϕ_G, θ_G, ψ_G, Z_G, U_G, and V_G represent angular and translational motion of the coarse gimbal side of the vernier assembly.

The axial proximeter signals $\hat{g}_A$, $\hat{g}_B$, and $\hat{g}_C$ combine electronically to compute the relative axial motion of the payload $\hat{Z}_R$ and the relative tilt of the payload $\hat{\phi}_R$ and $\hat{\theta}_R$. Relative translations $\hat{Z}_R$, $\hat{U}_R$, and $\hat{V}_R$ provide centering of the payload plate relative to the coarse gimbal side of the vernier using compensation like Eqs. (18c) and (18d). The vernier pointing and roll axes are controlled by inertially referenced feedback and command signals using compensation like Eq. (18a).

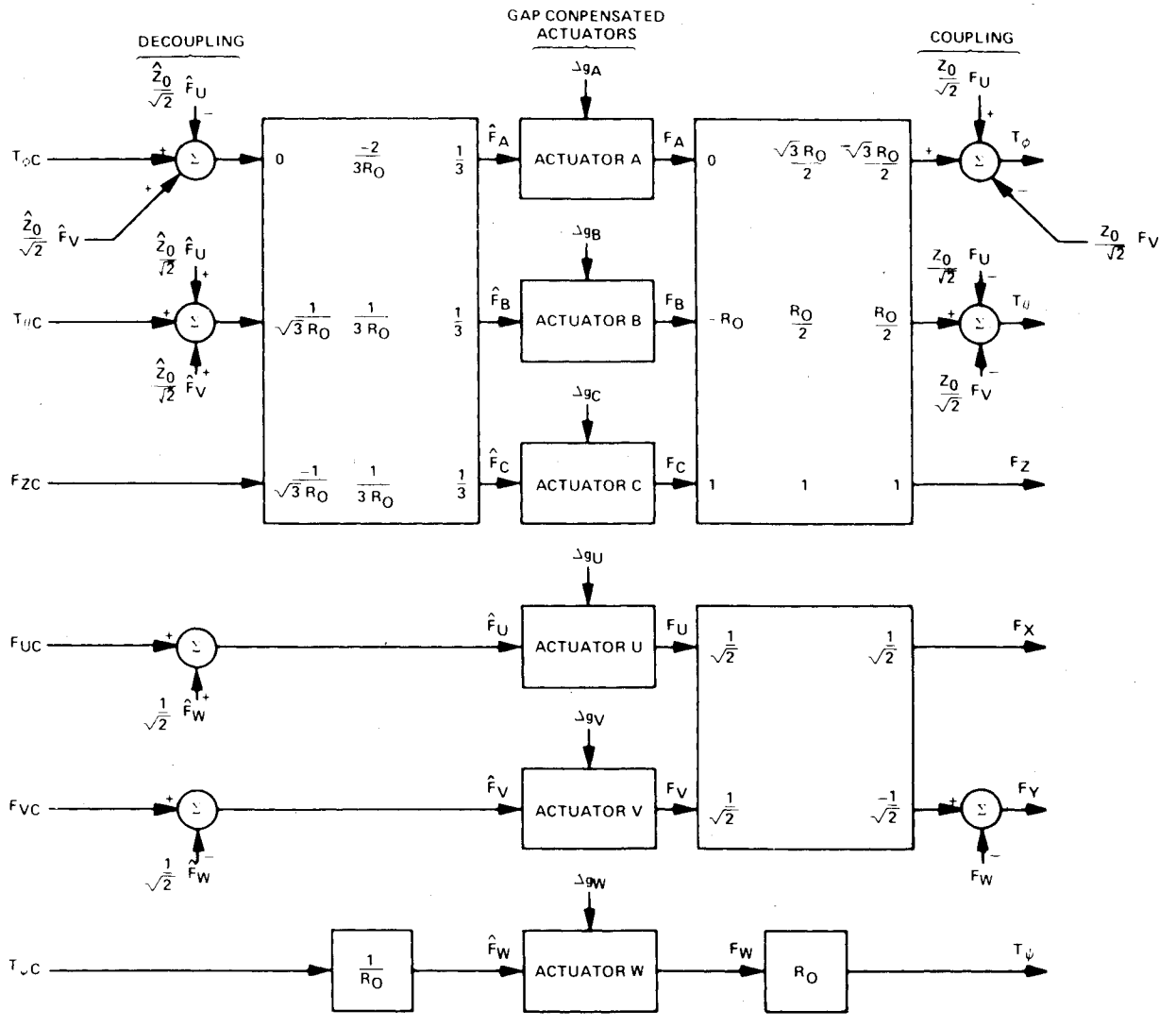

Fig. 8 Vernier actuator force and moment relationships.

The lateral gimbal is used in a followup mode driven by the yaw tilt $\hat{\phi}_R$, using compensation like Eq. (18b). Similarly, elevation is controlled by the pitch tilt $\hat{\theta}_R$. Due to the offset gimbal geometry, however, the inertia seen by the elevation gimbal varies with the lateral gimbal angle. This effect is compensated by varying the elevation proportional gain with a lateral angle correction factor in the software.

Slew Control System

Slew mode of control in the ASPS rapidly repositions the system at a new target within the acceleration and rate constraints of the system. This mode does not use inertial feedback from the payload for control, but relies instead on the built-in resolvers for elevation, lateral, and roll reference. (The attitude determination system continues to perform the strapdown computations required to maintain the payload reference in this mode, however.) It is anticipated that initial acquisition of a stellar or solar target for platform erection and calibration will utilize the slew mode.

During slew, the vernier tilt and gap translations must be held reasonably tight to prevent touchdown or dynamic interaction with the gimbals. Referring to the simple planar model of Fig. 3 with the dynamics listed in Eq. (1), the obvious approach is to control the vernier rotation and translational servos with the proximeter measured tilt and gap:

$$T_G = G_G(\sigma_{CMD} - \sigma_G) \tag{19a}$$

$$T_A = G_A(\sigma_S - \sigma_G) \tag{19b}$$

$$F_{AX} = G_{AX}(X_S - Z_{AS}\sigma_S - Z_{GA}\sigma_G) \tag{19c}$$

$$F_{AZ} = G_{AZ}(Z_S) \tag{19d}$$

This approach leads to control problems, however, in that strong coupling occurs between gimbal rotation, vernier rotation, and radial centering degrees of freedom. The situation is considerably worse in slew than in fine pointing because all of the control servos use relative position feedback signals. A large separation (greater than 10 to 1) must be provided to prevent the lead and lag frequencies used to stabilize one control loop from overlapping the compensation in another servo.

A better approach employs force and moment decoupling. Omitting the axial centering control, which is inherently decoupled,

$$T_G = G_G(\sigma_{CMD} - \sigma_G) - \hat{T}_A - \hat{Z}_{GA}\hat{F}_{AX} \tag{20a}$$

$$T_A = G_A(\sigma_S - \sigma_G) + \hat{Z}_{AS}\hat{F}_{AX} \tag{20b}$$

$$F_{AX} = G_{AX}(X_S - Z_{AS}\sigma_S - Z_{GA}\sigma_G) \tag{20c}$$

Substituting Eq. (20) into Eq. (1) and assuming perfect decoupling ($\hat{Z}_{AS} = Z_{AS}$, etc.),

$$I_G s^2 \sigma_G = G_G(\sigma_{CMD} - \sigma_G) \tag{21a}$$

$$I_S s^2 \sigma_S = G_A(\sigma_G - \sigma_S) \tag{21b}$$

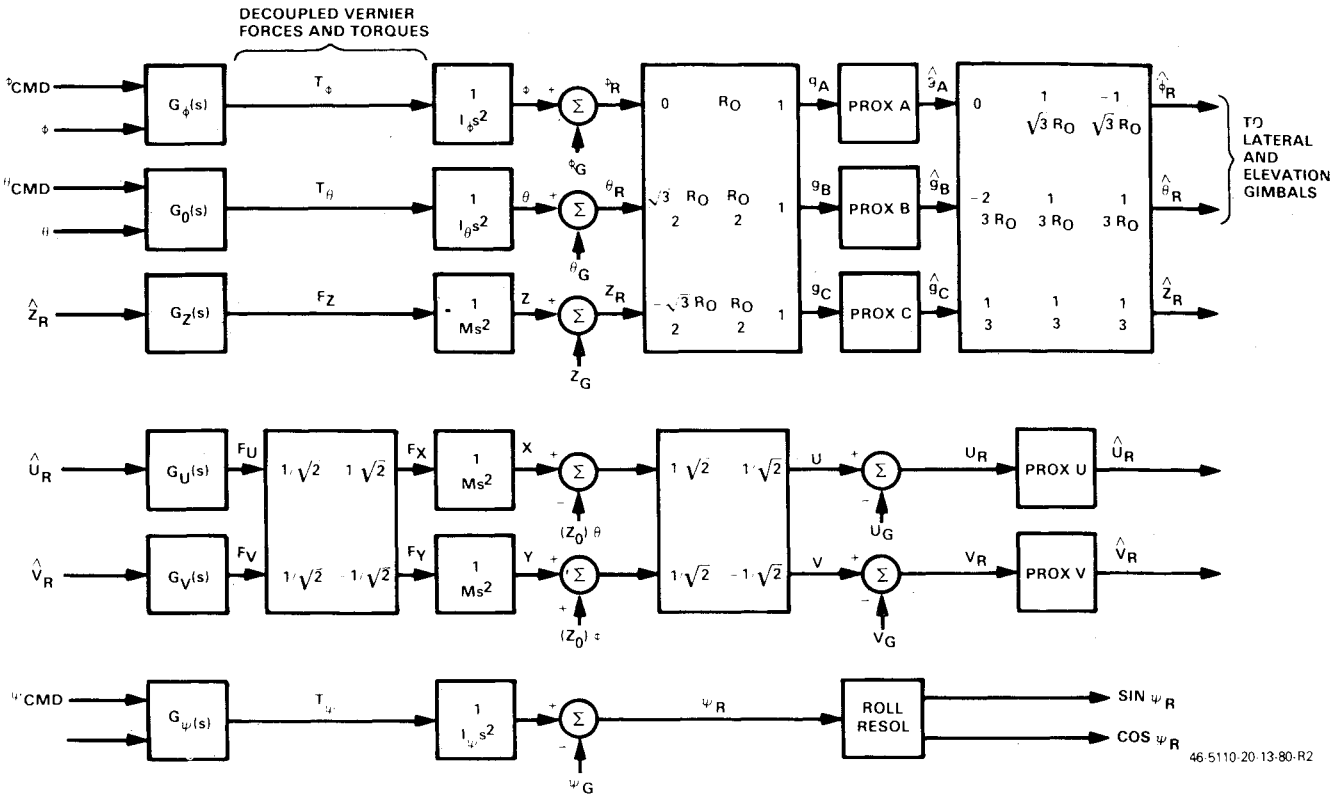

Fig. 9 Vernier control—fine-pointing mode.

Table 5 Slew mode control law parameters

Control loop	Bandwidth, Hz	Control law	K_p	τ_1	τ_2
Gimbal pointing	1	Eq. (26a)	$4.108\,I_G$	0.9869	0.06167
Vernier followup	10	Eq. (26b)	$410.8\,I_S$	0.09869	0.006167
Vernier radial and axial	10	Eqs. (26c) and (26d)	$410.8\,M_S$	0.09869	0.006167

$$M_S s^2 X_S = G_{AX}(-X_S + Z_{AS}\sigma_S + Z_{GA}\sigma_G) \tag{21c}$$

It is interesting to note that while a coupling exists between σ_G, σ_S, and X_S due to the relative sensing of the proximeters, this coupling is only in one direction; i.e., σ_S and X_S do not couple into $\ddot{\sigma}_G$, and X_S does not couple into $\ddot{\sigma}_G$ or $\ddot{\sigma}_S$. Therefore, the compensation can be designed independently for each axis of control.

The control laws for slew can be further improved by considering the relationship desired for an aligned slew. From Eq. (2),

$$\ddot{\sigma}_S = \ddot{\sigma}_G \tag{22a}$$

$$\ddot{X}_S = (Z_{GA} + Z_{AS})\ddot{\sigma}_G \tag{22b}$$

With force and moment decoupling, the gimbal acceleration is simply

$$\ddot{\sigma}_G = (G_G/I_G)(\sigma_{CMD} - \sigma_G) \tag{23}$$

Therefore, the control laws can be modified to include an acceleration feedforward:

$$T_G = G_G(\sigma_{CMD} - \sigma_G) - \hat{T}_A - \hat{Z}_{GA}\hat{F}_{AX} \tag{24a}$$

$$T_A = G_A(\sigma_S - \sigma_G) + \hat{Z}_{AS}\hat{F}_{AX} - (\hat{I}_S/\hat{I}_G)G_G(\sigma_{CMD} - \sigma_G) \tag{24b}$$

With perfect estimation of the dimensional and mass parameters, Eqs. (1) and (24) combine to give

$$I_G s^2 \sigma_G = G_G(\sigma_{CMD} - \sigma_G) \tag{25a}$$

$$I_S s^2(\sigma_S - \sigma_G) = G_A(\sigma_G - \sigma_S) \tag{25b}$$

$$M_S s^2(X_S - Z_{AS}\sigma_S - Z_{GA}\sigma_G) = G_{AX}(-X_S + Z_{AS}\sigma_S + Z_{GA}\sigma_G) \tag{25c}$$

which shows that the vernier pointing and centering feedback servos operate only to correct errors in the feedforward or decoupling terms.

Parameter selection for the gains and time constants of the slew mode compensation depends on payload characteristics and mission requirements. Typical values are given in Eqs. (26):

$$G_G(s) = K_{PGS}\left(\frac{\tau_{1GS}s + 1}{\tau_{2GS}s + 1}\right) \tag{26a}$$

$$G_A(s) = K_{PAS}\left(\frac{\tau_{1AS}s + 1}{\tau_{2AS}s + 1}\right) \tag{26b}$$

$$G_{AX}(s) = K_{PAXS}\left(\frac{\tau_{1AXS}s + 1}{\tau_{2AXS}s + 1}\right) \tag{26c}$$

$$G_{AZ}(s) = K_{PAZS}\left(\frac{\tau_{1AZS}s + 1}{\tau_{2AZS}s + 1}\right) \tag{26d}$$

The control law gains and time constants for the slew mode are shown in Table 5.

The extension of these control laws to the full eight-degree-of-freedom ASPS is straightforward and uses the same proximeter processing and vernier actuator force distribution as in fine pointing. Elevation gimbal axis inertia compensation is also made. However, an important difference exists in the manner in which the angular errors for the elevation, lateral, and roll axes are computed. In the slew mode, the software computes the sine and cosine of the commanded gimbal angles. These commands are then converted to ac voltages which are applied to the sine and cosine resolver windings. The rotor winding voltage is proportional to the sine of the error between command and actual angles. This voltage is demodulated and compensated to form the torque command. Use of the resolvers in an error computing mode is necessary to permit proper scaling of the error signal through the analog-to-digital (A/D) converters. For a 12-bit A/D and D/A converter, the command resolution will be $\pm\tan^{-1}(2^{-12}) = \pm 0.84$ arc-min, but the quantization of the feedback signal is much lower. For example, if the resolver error signal is scaled for 1-deg maximum, the gimbal angle feedback quantization is only $\sin^{-1}(2^{-11}\sin 1\ \text{deg}) = 1.76$ arc-sec.

Conclusions

System design studies indicate that the ASPS is a feasible pointing system capable of providing performance which will be limited by the accuracy of the attitude determination system and the range of the Shuttle disturbances. The 0.01 arc-sec vernier pointing stability requirement is the driving requirement for the control system design. This requirement applies to the peak transient error during Shuttle disturbances such as Shuttle vernier reaction control system (VRCS) limit cycle reaction jet impulses and man pushoff disturbances. System simulation studies indicate that the peak transient pointing error can be kept less than 0.01 arc-sec, if perfect sensors are employed. These studies assume the Shuttle VRCS and man pushoff disturbances which are presented in Ref. 7.

The ability to meet the pointing stability requirement with real sensors will primarily be determined by the noise and $\Delta\theta$ pulse quantization of the DRIRU-II strapdown inertial reference unit which is the short-term reference for the attitude determination system. The present DRIRU-II design has a 0.05 arc-sec pulse quantization in the low-rate mode. The possibility of reducing this quantization level is under investigation. Also, the use of a Kalman filter in the attitude determination system is being investigated. It would provide the optimum means of updating the DRIRU-II derived attitude by payload sensor data (sun sensor, star tracker, etc.) and account for the noise characteristics of the sensors.

Acknowledgments

The research discussed herein was supported by NASA Langley Research Center under Contract NAS1-14214.

References

[1] Anderson, W.W. and Groom, N.J., "The Annular Momentum Control Device (AMCD) and Potential Applications," NASA TN D-7866, 1975.

[2] Anderson, W.W. and Joshi, S.M., "The Annular Suspension and Pointing (ASP) System for Space Experiments and Predicting Pointing Accuracies," NASA TR R-448, 1975.

[3] Anderson, W.W. and Groom, N.J., "Magnetic Suspension and Pointing System," U.S. Patent 4,088,018, May 9, 1978.

[4] Anderson, W.W., Groom, N.J., and Woolley, C.T., "The Annular Suspension and Pointing System," AIAA Paper 78-1310, Palo Alto, Calif., Aug. 1978.

[5] "Space Shuttle Experiment Pointing Mount (EPM) Systems, An Evaluation of Concepts and Technologies," Jet Propulsion Lab., Pasadena, Calif., JPL Rept. No. 701-1, April 1, 1977.

[6] Cunningham, D.C., Gismondi, T.P., and Wilson, G.W., "System Design of the Annular Suspension and Pointing System (ASPS)," AIAA Paper 78-1311, Palo Alto, Calif., Aug. 1978.

[7] "Space Shuttle System Payload Accommodations," NASA Rept. JSC 07700, Vol. XIV, Revision C, July 3, 1974.